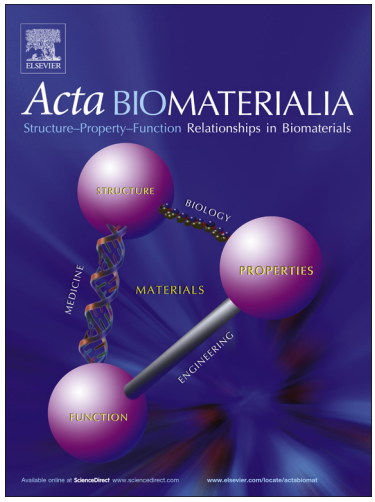

Full length article

Angiogenesis impairment by the NADPH oxidase-triggered oxidative stress at the bone-implant interface: critical mechanisms and therapeutic targets for implant failure under hyperglycemic conditions in diabetes

Xiao-Fan Hu, Lin Wang, Geng Xiang, Wei Lei, Ya-Fei Feng

PII: S1742-7061(18)30198-3
DOI: https://doi.org/10.1016/j.actbio.2018.04.008
Reference: ACTBIO 5408

To appear in: *Acta Biomaterialia*

Received Date: 12 January 2018
Revised Date: 25 March 2018
Accepted Date: 3 April 2018

Please cite this article as: Hu, X-F., Wang, L., Xiang, G., Lei, W., Feng, Y-F., Angiogenesis impairment by the NADPH oxidase-triggered oxidative stress at the bone-implant interface: critical mechanisms and therapeutic targets for implant failure under hyperglycemic conditions in diabetes, *Acta Biomaterialia* (2018), doi: https://doi.org/10.1016/j.actbio.2018.04.008

Angiogenesis impairment by the NADPH oxidase-triggered oxidative stress at the bone-implant interface: critical mechanisms and therapeutic targets for implant failure under hyperglycemic conditions in diabetes

Xiao-Fan Hu [1], Lin Wang [1], Geng Xiang [1], Wei Lei *, Ya-Fei Feng *

Department of Orthopedics, Xijing Hospital, The Fourth Military Medical University, Xi'an, 710032, People's Republic of China

Corresponding authors: Department of Orthopedics, Xijing Hospital, The Fourth Military Medical University, Xi'an 710032, People's Republic of China. Tel: +86-029-84771011.

E-mail address: fengyafei2005@163.com (Y.-F. Feng), leiwei@fmmu.edu.cn (W. Lei).

[1] These authors contribute equally to this work.

(7719 words in the main text, 47 typed pages, 1 table, 11 figures, 1 graphical abstract and 1 supplementary material)

Abstract

Mechanism underlying the diabetes-induced poor osteointegration of implants remains elusive, making it a challenge to develop corresponding solutions. Here, we studied the role of angiogenesis in the diabetes-induced poor bone repair at the bone-implant interface (BII) and the related mechanisms. In vivo, titanium screws were implanted in the femurs of mice, and, in vitro, vascular endothelial cell (VEC) was cultured on titanium surface. Results showed that, compared with normal milieu (NM), diabetic milieu (DM) led to angiogenesis inhibition around implants which resulted in reduced osteoprogenitors and poor bone formation on BII in vivo. In vitro, DM caused significant increase of NADPH oxidases (NOX), dysfunction of mitochondria and overproduction of reactive oxygen species (ROS) in VEC on titanium surface, inducing obvious cell dysfunction. Both Mito-TEMPO (Mito, a mitochondria-targeted ROS antagonist) and apocynin (APO, a NOX inhibitor) effectively attenuated the oxidative stress and dysfunction of VEC, with the beneficial effects of APO significantly better than those of Mito. Further study showed that the diabetes-induced metabolic disturbance of VEC was significantly related to the increase of advanced glycation end products (AGEs) at the BII. Our results suggested that the AGEs-related and NOX-triggered cellular oxidative stress leads to VEC dysfunction and angiogenesis impairment at the BII, which plays a critical role in the compromised implant osteointegration under diabetic conditions. These demonstrated new insights into the BII in pathological states and also provided NOX and AGEs as promising therapeutic targets for developing novel implant materials to accelerate the

angiogenesis and osteointegration of implants in diabetic patients with hyperglycemia.

Keywords: Angiogenesis; Bone-implant interface; Diabetes; Oxidative stress; NADPH oxidase; AGEs

1. Introduction

Orthopedic and dental implants have been used successfully for decades to replace or repair missing or damaged bones, joints, and teeth, thereby restoring patient function subsequent to disease or injury [1, 2]. However, although the use of many modern biomaterials, especially metallic materials, for endosseous implants have been evolving for the last 60 years, their clinical performance are dramatically limited in some disease conditions, especially diabetes [3-5]. Both clinical and preclinical studies have observed that diabetic milieu (DM) leads to poor bone regeneration on bone-implant interface (BII) and compromised osteointegration of implants, resulting in much higher failure rates ranging from 10% - 20% in diabetic patients with hyperglycemia than that of 1% - 3% in normal patients [5-7]. Such implant failure could cause excruciating complications and even death, making diabetes a major contraindication for the clinical application of implant materials [1]. Unfortunately, according to the annual report from international diabetes federation in 2017 [8], every 1 in 11 adults on the earth have diabetes (425 million), which number is predicted to be 642 million by 2040. By now, the mechanism underlying this diabetes-induced implant failure is still far from clear, making it a challenge to develop corresponding therapeutic strategies, such as the innovation of implant materials.

A critical component in bone healing and implant osteointegration is the timely appearance of blood vessels in the repair sites on BII, which supplies oxygen,

nutrients, stem cells able to differentiate into osteoblasts and also the ions necessary for mineralization such as calcium ion and phosphate [9, 10]. Angiogenesis, namely the formation of new blood vessels, closely couples with osteogenesis in bone development and repair [9, 11]. Diabetes, however, causes various vascular complications and inhibits angiogenesis in wound healing [12, 13]. The diabetic vascular abnormalities have been shown to be quite different among different organs, with reduced vasculature in some organs like heart but obvious vascular hyperplasia in eyes and kidney [12]. By now, the changes of bone blood vessels in diabetes are still poorly understood, with conflicting results reported [14, 15]. In addition, on bone-implant interface (BII), which is a special bio-environment subjected to the interaction between implants and the host tissue [16, 17], the influence of DM on angiogenesis and the mechanism underlying such influence are still unclear.

Increasing evidence indicates that the production of oxidants and the cellular response to oxidative stress are intricately connected to the fate of implanted biomaterials [18, 19]. It has been demonstrated that diabetes-mediated accumulation of reactive oxygen species (ROS) may deleteriously affect the bone regeneration on BII, leading to compromised implant osteointegration [20]. However, how does ROS impact the biological process on BII and how does DM induce such excess of ROS still need further investigation. Vascular endothelial cell (VEC) serves as the key executor and regulator of vascular functions [21]. Evidence from both the bench and the bedside have shown that DM causes ROS overproduction in VEC, resulting in cellular

oxidative stress which has been accepted as an important mechanism underlying the diabetic vascular complications in organs like heart and kidney [12, 13]. On BII, however, the role and mechanism of ROS in the DM-induced influence on angiogenesis remain elusive.

Mitochondria and NADPH oxidases (NOX) are the two main sources for ROS in VEC [22]. Our previous work suggested that mitochondrial dysfunction might be a critical mechanism underlying the DM-induced ROS overproduction in osteoblasts on the surface of titanium implant [23]. Nevertheless, the exact roles of mitochondria and NOX in the oxidative stress of cells on the interface have not been clearly elucidated, especially in VEC.

Therefore, the aims of the present study were to investigate: (1) the influence of diabetes on the angiogenesis on BII and its role in the poor osteointegration of implants; (2) the mechanisms underlying such influence, especially about the role of ROS; (3) the molecular and cellular mechanisms underlying the diabetes-induced ROS overproduction on BII, about mitochondria and NOX specifically.

2. Materials and methods

2.1. Preparation of Ti6Al4V specimen

Ti6Al4V alloy was machined into circular disks (10 mm in diameter and 1 mm in thickness) and screws (1 mm in diameter, 2.5 mm in length and 0.1 mm in thread pitch) in Northwest Institute for Nonferrous Metal Research, Xi'an, China. Circular disks were used in experiments in vitro and screws in study in vivo. Titanium disks were first polished with 1000- to 7000-grit SiC sandpaper and then subjected to ultrasonic washing (ethanol and de-ionized water in sequence for 15 min each).

2.2. Animal surgery and treatments

The animal experiments were carried out in strict accordance with the National Institutes of Health Guidelines for the Use of Laboratory Animals and the guidelines of the Fourth Military Medical University (Approval number from Animal Ethical Committee: FMMU-AEEA-20160903). For the introduction of diabetes model, adult C57BL/6 mice (male, 10-week old) received a 12-hour fasting and then intraperitoneal injection of streptozotocin (50 mg/Kg; Sigma-Aldrich, St Louis, MO, USA) dissolved in citrate buffer (pH 4.5) for two times every two days. After regular monitoring of blood glucose level every 5 days, the mice with blood glucose levels higher than 11.1 mmol/L were regarded as diabetic [24].

Implantation surgery was conducted as we previously described [23], with titanium screws implanted in the right femurs of mice. Normal mice were used in control group and diabetic mice were randomly divided into three groups (n = 20 per group): DM

group, DM + Apocynin (APO, an inhibitor of NADPH oxidases, Selleckchem, Houston, USA) group and DM + sRAGE (The soluble form of receptor for advanced glycation end products (AGEs), a decoy receptor, R&D Systems, Minneapolis, MN, USA). Before suturing the incision, we injected 20 μl of APO (20 μM) or sRAGE (100 μg/ml) into the mid-diaphysis of the surgical-side femurs of DM mice with a 0.4-mm needle [25]. After that, the same doses of APO or sRAGE were injected to the periosteum of the distal femur every 4 days. 2 and 8 weeks after implantation surgery, mice were sacrificed and the distal half of femurs were harvested for the following experiments.

2.3. Analysis of the angiogenesis and osteoprogenitors on BII

2.3.1. Immunofluorescent histochemistry

2 weeks after implantation surgery, mice (n = 6 per group) were sacrificed and femur specimens were obtained. After being fixed in 10% formalin solution for 12 h at 4℃, the specimens were decalcified in 10% EDTA (Sigma) solution for 4 days. Two incisions, paralleled with the major axis of the screw, were made respectively on the ventral and dorsal sides of the femur. At the crevice of incisions, bone tissue surround the implant was carefully divided into two parts and forced apart from the implant surface, minimizing the damage of the interface tissues. After being immersed in 30% (w/v) sucrose in 0.1 M phosphate buffer (PB, pH 7.3) overnight at 4℃, the bone tissue were cut in a cryostat (Leica CM1800; Heidelberg, Germany) to transverse sections (35 μm). Sections were processed for standard immunofluorescent

histochemical staining and analysis as previously described [26], with primary antibodies, goat anti-endomucin (EMCN, an endothelial cell marker; R&D Systems) and rabbit anti-osterix (OSX, an osteoprogenitor marker; Abcam, Cambridge, England), as well as secondary antibodies to corresponding species conjugated with Alexa 488 or 594 (Millipore, Billerica, MA, USA). Cell nucleus was stained with 40, 60-diamidino-2-phenylindole (DAPI, Sigma). After being air-dried and coverslipped, the sections were observed under a confocal laser scanning microscope (FV-1000, Olympus, Tokyo, Japan) with the appropriate laser beams and filter settings, and confocal images were captured. For quantitative analysis of the angiogenesis and osteoprogenitors around implants, a region of interest (ROI) was defined as a ring around the screw extending 200 μm from the lowest point of the thread grooves and barring the region of screw threads (Fig. 2E). The area ratio of blood vessels (labeled by EMCN) and the total number of OSX+ osteoprogenitors in the ROI were determined with Image J software version 1.43 (for details, please see Fig. S1). 4 nonadjacent slices of each sample were analyzed, with 5-6 samples in each group.

2.3.2. Real-time Quantitative PCR (qPCR)

Bone tissue around the implants were collected at 2 weeks after surgery (n = 5-6 per group) to evaluate the gene expressions of EMCN (endomucin), Vegf-a (vascular endothelial growth factor A), Nog (noggin), Bmp-2 (bone morphogenetic protein 2), Runx2 (runt related transcription factor 2) and Osterix (Sp7 transcription factor) by qPCR. RNA isolation from the tissue was performed using Trizol (Life

Technologies, Carlsbad, CA, USA) and RNeasy Mini kit (Qiagen, Germantown, MD, USA) according to the manufacture's instruction and as described previously [27]. The extracted RNA samples were then reversely transcribed for the first strand cDNA synthesis, which was used to perform real-time PCR with Bio-Rad CFX Manager system. The primers used in this study were from PrimerBank database and listed in Table 1. β-actin was used as a housekeeping gene.

2.4. New bone formation around implants in vivo

2.4.1. Fluorochrome label of new bone mineralization

After surgery, animals were subcutaneously injected with calcein (10 mg/kg, Sigma) at 2 weeks and alizarin complexone (20 mg/kg, Sigma) at 4 weeks. At 8 weeks, mice (n = 7 per group) were sacrificed, and femur specimens were obtained. After fixation in 10% formalin solution for 4 days, the specimens were assessed firstly by Micro-CT analysis and then by histological analysis. In histological analysis, the specimens were dehydrated in a graded series of ethanol (70%-100%) and embedded in methylmethacrylate (Sigma) solution that polymerized at 37℃ within 7 days. In an interlocked diamond saw (Leica Microtome, Wetzlar, Germany), thin sections (50 μm in thickness) were prepared. The sections were observed with a fluorescent microscope (Olympus), with images obtained and analyzed by Image J software to get the ratio of bone formation area to the total area (BFA/TA) in the ROI. For quantitative analysis, 3 slices of each sample were analyzed, with 6-7 samples in each group.

2.4.2. Micro-CT evaluation

Specimens (n = 7 per group) were scanned in a Micro-CT system (Y.Cheetah X-ray, Y.XLON, Germany; 90 kV, 50 μA and 600 ms integration time) and images were reconstructed with an isotropic voxel size of 5 μm. To discriminate bone from other tissues, a multi-level thresholds procedure was applied in data analysis (threshold for bone = 350 and implant = 1200). The ROI included a ring radius 200 μm from the implant surface (Fig. 2D and E, yellow). In the ROI, 3D-reconstructed images of the newly formed bone around implants were processed and the bone volume per total volume (BV/TV) was assessed.

2.5. Cell culture on the surface of titanium alloy

Human Umbilical Vein Endothelial Cells (HUVEC, named as VEC), purchased from American type culture collection (ATCC, Manassas, VA, USA), were cultured in Dulbecco's modified Eagle's medium (DMEM, Gibco, USA) supplemented with 10% fetal bovine serum (FBS, Gibco), 50 U/ml heparin (Selleckchem), 1% penicillin (Gibco) and streptomycin (Gibco). HUVECs at passages between 4 and 7 were used in all experiments to be seeded on the specimens with 1×10^4 cells/ml and randomized to incubate with normal milieu (NM) or diabetic milieu (DM) in 24-well plates. The culture media were changed every other day. Completed culture media containing 25 μM glucose (Sigma) and 500 μM BSA-conjugated palmitate (Sigma) was used as the mimic milieu of diabetes (high glucose and fat) [28] and labeled as

‘‘DM”. Additional drugs, namely Mito-TEMPO (Mito, a mitochondria-targeted ROS antagonist, 10 μM, Sigma), apocynin (APO, 20 μM, Selleckchem), AGE (AGE-BSA, 100 μg/ml, please see section 2.12.2.), sRAGE (5 μg/ml, R&D Systems) and aminoguanidine (Ami, an inhibitor of AGEs formation, 500 μM, Selleckchem), were added into the culture media according to the experimental design.

2.6. Cell adhesion and morphology on titanium

Vinculin, a multi-domain adaptor protein in focal adhesion plaques, serves as a key regulator of focal-adhesion formation and cell adhesion. To evaluate the adhesion of VEC on titanium surface, 3 days after incubation, VEC were fixed by 4% paraformaldehyde, stained with primary antibody against vinculin (R&D Systems), and visualized using Alexa Fluor 488-conjugated secondary antibody (Invitrogen, Eugene, OR, USA). Cellular actin filaments and nucleus were stained respectively with Rhodamine-phalloidin (Molecular Probes, Eugene, OR, USA) and DAPI (Sigma) as we reported previously. Fluorescent images were obtained by a confocal microscope. The cell area and cell density were measured using the Image J software. Six different substrate fields were measured per sample, and three separate samples were measured in each group.

After incubation for 3 days, cellular micro-morphology was observed using the scanning electron microscope (SEM, S-4800, Hitachi, Japan) operating at 5 kV and a semiautomatic interactive image analyzer. Before observation, the samples were fixed

in 2% (v/v) glutaraldehyde (Sigma) at 4℃ overnight, dehydrated through an ethanol series, critical-point dried, and sputtered with gold lastly.

2.7. Cell proliferation

After 7 days of incubation, the proliferation of VEC was assessed by methylthiazol tetrazolium (MTT) test (Beyotime Biotechnology, Shanghai, China) and immunofluorescent staining of Ki-67 (Invitrogen), a cell proliferation marker, as previously described [29, 30]. The cell proliferation in MTT assay was expressed as the absorbance per gram of sample. Fluorescence images were obtained with a confocal microscope, after which the cell density and the percentage of Ki-67+ cells were measured using the Image J software.

2.8. Angiogenesis in vitro by tube formation test

A Matrigel tube-formation assay was performed to assess in vitro angiogenesis [31]. 7 days after incubation, VEC on titanium were trypsinized with 0.05% pancreatic enzyme, resuspended at 2×10^5 cells/mL with culture media containing 1% FBS and plated at 2×10^4 cells/well in 96-well plates precoated with growth factor-reduced Matrigel (BD, San Jose, CA, USA). After 5 - 6 hours, the tube formation by VEC on Matrigel surface was observed with microscope (Zeiss). Pictures in five fields were captured and counted for each well, with three wells detected for each group. The mean tube length per field was quantified with Image-Pro Plus software (Media Cybernetics, Silver Spring, USA).

2.9. Cell migration assessed by wound-healing assay

Wound-healing assay was performed as previously described with some adjustment [31, 32]. 7 days after incubation, VEC on implants were trypsinized, resuspended in DMEM containing 5% FBS, plated in 48-well plates at 2×10^5 cells/well and cultured for 12 h to form confluent cell monolayer in the wells. Confluent monolayers were serum starved for 2 h and then were wounded with a pipette tip. After three washes to remove the detached cells, the remaining cells were incubated in serum-starved medium. The cell-free wounds was recorded in four fields in each well using microscope (Axiovert D1, Zeiss), immediately (0 h) after wounding and 12 h later at the same place. The number of cells migrated into the wounds at 12 h were counted.

2.10. Evaluation of cellular oxidative stress

2.10.1. Measurement of intracellular ROS in vitro

Intracellular ROS level was evaluated by detecting the intensity of 2',7'-dichlorofluorescein (DCF) fluorescence and lipid peroxidation level [23]. On day 7, VEC were digested, washed with PBS and incubated with 10 μmol/L 2',7'-dichlorofluorescein diacetate (DCFH-DA, Sigma) diluted in phosphate-buffered saline (PBS) for 30 min at 37 ℃. When oxidized by ROS, the nonfluorescent DCFH-DA is converted to the highly fluorescent DCF. After being washed with PBS for three times, the relative fluorescence levels were quantified using flow cytometry (FACS Aria II, Becton Dickinson, San Jose, CA, USA) at an excitation wavelength of

488 nm and an emission wavelength of 525 nm. 1×10^5 cells were measured in each analyzed sample. To observe the intracellular ROS level directly, cells on titanium surface were washed with PBS and incubated with 10 μmol/L DCFH-DA at 37 ℃ for 30 min, after which the DCF fluorescence was observed by a confocal microscope and images were obtained.

Malondialdehyde (MDA), a secondary product of lipid peroxidation caused by oxidative free radicals and a biomarker of oxidative damage, was measured as thiobarbituric acid-reactive substances (TBARS). The TBARS concentration in the cell culture supernatants was determined as described previously [33]. Briefly, 200 μl cell homogenate were prepared by Triton X-100 lysis buffer and then analyzed with the TBARS Assay Kit (Cell Biolabs, San Diego, CA, USA). TBA reacts with the MDA to form a TBARS diadduct which is a pink chromogen detectable at 532 nm.

2.10.2. Western blot analysis

7 days after incubation, the protein levels of a key oxidase, NOX2, in VEC was evaluated by western blot analysis with primary antibodies against NOX2 (Cell Signaling Technology, Beverly, MA, USA) and normalized to the levels of β-actin. For each group, protein expression was determined from 3 samples, with each sample tested 3 times by western blot analysis (9 bands for each group). For quantitative analysis, the levels of target proteins were normalized against that of β-actin. In each group, the 9 normalized protein levels were calculated to get an intragroup mean and a

standard error (SEM). Then the mean of NM group was set as a ‘‘standard”, and data from other groups were divided by this standard to get the fold changes.

2.10.3. Immunohistochemical evaluation of ROS on the BII in vivo

8-OHdG (8-hydroxy-20-deoxyguanosine, a marker of DNA damage in oxidative stress) in bone sections was visualized by immunohistochemical staining with primary antibody (Abcam) as we previously described [23]. For semi-quantification analysis, 3 samples were analyzed in every group, with 4 slices evaluated in each sample. The number of 8-OHdG-positive cells in the ROI around implants was counted.

2.11. Determination of mitochondrial function

2.11.1. Intracellular ATP assay

After 7 days of incubation, culture supernatant was removed and cells on titanium surface were gently washed twice with PBS. After that, ATP level in the VEC was measured using luminescence ATP detection assay (ATPlite, PerkinElmer, USA) according to manufacturer's instructions [34]. Data were measured with a microplate reader, reported as arbitrary luminometric units (a.u.) and normalized by protein content.

2.11.2. Analysis of mitochondrial membrane potential (MMP)

The ratiometric dye, JC-1 (Mitoprobe, Invitrogen) was used to estimate the MMP, according to the manufacture’s instruction and as described previously [35]. JC-1 is a

cationic dye that exhibits potential-dependent accumulation in mitochondria, indicated by a fluorescence emission shift from green (~525 nm) to red (~590 nm). Mitochondrial depolarization is indicated by a decrease of the red/green fluorescence ratio. On day 7, culture supernatant was removed and cells were gently washed twice with PBS. Then cells were incubated with JC-1 dye (5 μg/ml) diluted in non-serum culture media at 37°C for 30 min, protected from light. After washing for 3 times with PBS to remove the redundant dye, the fluorescence in cells was immediately analyzed using GloMax plate reader (Promega, USA). Red fluorescence was measured at 525/630 nm and green fluorescence at 490/530, with data presented as the mean of the red/green fluorescence ratio. Images of JC-1-treated cells were acquired by a confocal microscope to directly show the red/green fluorescence in cells.

2.12. Experiments about advanced glycation end products (AGEs)

2.12.1. Determination of the levels of AGEs and receptor for AGEs (RAGE) in vitro and vivo

7 days after incubation, ELISA kits (LifeSpan BioSciences, Seattle, WA, USA) were used to determine the levels of two representative AGEs, pentosidine and N^{ε}-carboxymethyllysine (CML), in VEC on implants [36]. Briefly, cell media were removed and cells on implants were washed 3 times with PBS. After lysed in 1 ml RIPA buffer on ice for 10 min, the cell lysates were tested by ELISA assay according to manufacturer's instructions. At the same time, the level of CML in culture supernatant was also determined. Protein levels of RAGE in cells were detected by

Western blotting analysis with a goat anti-RAGE primary antibody (R&D Systems) and normalized to the levels of β-actin. In vivo, the level of AGEs on the interface was assessed by immunohistochemical evaluation with primary antibodies against AGEs (Novus Biologicals, Littleton, CO, USA).

2.12.2. Preparation of AGE

AGE was self-made by exposing albumin (BSA, bovine serum albumin) to glucose for a long time [37]. BSA (Sigma) at 50 mg/ml was incubated under aseptic conditions with 0.5 mol/L glucose in PBS (pH 7.4, containing protease inhibitors and antibiotics) at 37°C for 6 weeks to form AGE-BSA. Control proteins were exposed to the same buffer (without glucose) at 37°C for the same time interval. The unincorporated sugars were removed utilizing dialysis against PBS. Endotoxin levels in the AGE-BSA were tested by an endotoxin testing kit (Limulus J Single Test, Wako Pure Chemical Industries, Osaka, Japan). AGE-BSA solution at the concentration used for cell culture in this study, 100 μg/ml, was shown to be endotoxin-free (< 2.5 U/ml of endotoxin).

2.13. Statistics

The data were presented as means ± SEM. For each group, at least three independent experiments were conducted with duplicate sample. Statistical analysis was done with a one-way ANOVA followed by Bonferroni's multiple comparison test. $P < 0.05$ was considered statistically significant.

3. Results

3.1. Diabetes led to impaired angiogenesis on bone-implant interface (BII)

To evaluate the influence of diabetes on the angiogenesis on BII, screws made of titanium alloy which is the most-used material for endosseous implants in clinics, were implanted in the femurs of mice. The angiogenic responses on the interface were assessed 2 weeks after surgery. Immunofluorescent staining (Fig. 1A and D) showed that, compared with normal milieu (NM), there were markedly less tissue ingrowth into the backlash of screw threads (cell nucleus stained as blue) and less blood vessels (labeled by a VEC marker, EMCN, green [38]) around implants in diabetic milieu (DM). Histomorphometric analysis (Fig. S1) showed that the area ratio of blood vessels in the ROI around screws was significantly lower in diabetic animals than in control animals (4.82 ± 0.72% *vs.* 19.44 ± 1.51%, $p < 0.05$, Fig. 1B), which was further confirmed by qPCR analysis of the mRNA level of EMCN in the tissue around implants (Fig. 1C). The expressions of three representative crucial cytokines which mediate the intercellular communication between VEC and osteoblastic cells, VEGF-A, Noggin and BMP-2, were also significantly decreased in DM compared with in NM (Fig. 1F).

3.2. The diabetes-induced angiogenesis impairment led to poor bone repair on BII

To investigate the role of the angiogenesis inhibition in the compromised osteointegration on BII under diabetic conditions, we evaluated the behaviors of

osteoprogenitors around the implants 2 weeks after implantation. Immunofluorescent staining (Fig. 1D) showed that osteoprogenitors (labeled by Osterix (OSX), red) were mainly distributed around the blood vessels, consistent with the role of blood vessels as a key supporter and regulator of osteoblastic cells. Compared with NM group, the number of osteoprogenitors in the ROI (37.36 ± 4.21 *vs*. 253.72 ± 19.85, $p < 0.05$, Fig. 1E) and the expressions of two crucial osteogenic genes in osteoprogenitors, RUNX2 and Osterix (Fig. 1G), around implants were significantly lower in DM group. Correspondingly, the new bone mineralization (labeled by fluochrome, Fig. 2A) around implants was obviously less in DM than those in NM. The ratio of bone formation area to the total area (BFA/TA) in the ROI, calculated from the fluorochrome label, was decreased in DM (7.56 ± 1.21% *vs*. 33.16 ± 3.37%, $p < 0.05$, Fig. 2B). As a result, 8 weeks after surgery, micro-CT analysis showed the compromised osteointegration of titanium implants in DM compared with in NM, reflected by the much less bone tissue around implants (Fig. 2F) and the lower ratio of bone volume to total volume (BV/TV) in the ROI (9.37 ± 3.12% *vs*. 43.52 ± 4.96%, $p < 0.05$, Fig. 2C).

3.3. DM led to the dysfunction of VEC on titanium surface

To investigate the mechanism underlying the diabetes-induced angiogenesis inhibition on BII, we evaluated the influence of DM on the behaviors of VEC on titanium alloy surface. To evaluate cell adhesion, at day 3, VEC on titanium were stained by immunocytochemical staining. The cytoskeleton, vinculin (a protein in focal adhesion

plaques associated with cell-cell and cell-matrix junctions) and cell nucleus were stained as red, green and blue respectively (Fig. 3A). In NM, VECs extended their orderly cytoskeleton on the flat implant surface, with vinculin abundantly distributed in the region of cell-material contact. In DM, however, many cells showed twisted cytoskeleton (arrowheads) without good extension and even intracellular vacuoles (arrow). VEC in DM showed less vinculin, especially at the cell edge, which might account for the cytoskeletal disorganization because of the important role of vinculin in anchoring the actin cytoskeleton to the adhesion molecules on cell membrane. Quantitative analysis further showed that, compared with NM, DM induced decreased cell spreading area (874.3 ± 72.1 μm^2 *vs.* 2387.4 ± 210.1, $p < 0.05$) on titanium (Fig. S2). All these indicated that DM led to bad adhesion of VEC on titanium surface.

Cell morphology on implants was further observed with SEM after 3 days of incubation (Fig. 3B). In NM, VEC adhered to material surface and extended their cytoplasm into flat shape. Cells showed relatively straight filipodias anchoring to titanium and connecting between cells, and abundant microvillus on cell surface. However, cells treated with DM showed much less, shorter and curving pseudopodia as well as atrophied looking, with much less microvillus on cell surface.

Cell proliferation was assessed by MTT assay, the cell density on titanium and the immuofluorescent staining of Ki-67, a cellular marker for proliferation [30]. Compared with NM group, cell density (111 ± 13.7 cells/mm^2 *vs.* 427.3 ± 46.2, $p <$

0.05, Fig. 4A and C) on material surface and the percentage of Ki-67 positive cells (16.2 ± 2.0% *vs.* 57.4 ± 4.6%, $p < 0.05$, Fig. 4A and D) were significantly lower in DM group. MTT assay further showed a 72% decrease of cell proliferation in DM, compared with in NM (Fig. 4E).

Next, the in vitro angiogenesis and cell migration of VEC after 7 days of incubation on titanium were respectively tested by tube formation assay (Fig. 5A-C) and wound-healing assay (Fig. 5D and E). Results showed that, compared with NM group, DM group showed significantly less tube formation on Matrigel and less cell migration into the wounds of cell monolayer (135.2 ± 9.3 *vs.* 5.6 ± 0.9, $p < 0.05$).

3.4. Mitochondrial dysfunction contributed to the oxidative stress-induced dysfunction of VEC on implant surface

To investigate the mechanism underlying the DM-induced dysfunction of VEC, considering the critical role of oxidative stress on BII in the poor implant osteointegration in diabetes, we tested the levels of ROS in VEC on implants with the intensity of DCF fluorescence 7 days after incubation (Fig. 6A and B). Compared with NM group, DCF fluorescence intensity in the cells in DM group showed a four-fold increase (5.61 ± 0.48 *vs.* 1.00 ± 0.08, $p < 0.05$). The Malonaldehyde (MDA) level in VEC in DM was nearly five folds of that in NM (Fig. 6C). 14 days after surgery, immunohistochemical staining of bone sections further showed that the level of 8-OHdG, a marker for ROS-induced DNA damage, in the tissue around implants was

significantly higher in DM than in NM (Fig. 6D and F).

Next, we evaluated the status of mitochondria and NADPH oxidases (NOX), the two main sources for intracellular ROS, in VEC after 7 days of incubation. Western blot analysis showed that the protein level of NOX2, a representative member in NOX family which has be implicated in diabetic vascular injuries, showed a 1.5-fold increase in the VEC in DM than that in NM (Fig. 6E). The mitochondrial function of VEC was tested by the intracellular ATP production level (Fig. 7A) and mitochondrial membrane potential (MMP, Fig. 7B and C). DM led to a 76% reduction of ATP production (613.2 ± 79.2 a.u. *vs*. 2603.2 ± 155.7 a.u., $p < 0.05$) and significant decrease of MMP (8.2 ± 1.1 *vs*. 26.4 ± 2.3, $p < 0.05$) compared with those in NM, suggesting the diabetes-induced mitochondrial dysfunction in VEC on the interface.

However, in DM, the treatment with a mitochondria-targeted ROS antagonist, Mito-TEMPO, induced functional recovery of mitochondria (Fig. 7) and significant reduction of ROS in VEC (Fig. 6A-C) as well as obviously improved cell behaviors, evidenced by better cell adhesion (Fig. 3A), morphology (Fig. 3B), proliferation (Fig. 4), migration (Fig. 5D and E) and angiogenesis in vitro (Fig. 5A-C).

3.5. The diabetes-induced upregulation of NOX triggered the ROS overproduction and mitochondrial dysfunction in VEC on implant surface

Given the increase of NOX in VEC, we next used apocynin (APO), an inhibitor of

NOX, to investigate the role of NOX in the oxidative stress of VEC. In DM, APO treatment led to significant decrease of NOX2 (Fig. 6E) and ROS (Fig. 6A-C) in VEC as well as much better cell behaviors on implant surface (Figs. 3-5). Remarkably, the inhibiting effects of APO on the ROS level were significantly stronger than those of Mito-TEMPO, and the functional recovery of VEC induced by APO was also more prominent than that induced by Mito-TEMPO (labeled by & in Figs. 4-6). The beneficial effects of APO were further confirmed in vivo by the reduced 8-OHdG level (Fig. 6F), improved angiogenesis, increased osteoprogenitor activities (Fig. 1) and new bone deposition on BII (Fig. 2) in diabetic animals. Mitochondria is not only a critical source for ROS, but also an organelle susceptible to excess ROS. Following the reduction of ROS, the mitochondrial dysfunction was also mitigated by APO (Fig. 7).

3.6. The increase of AGEs on BII contributed to the metabolic stress of VEC and poor angiogenesis in diabetes

Next, we wanted to know what pathological factor in diabetes led to the metabolic disturbance of VEC and poor angiogenesis on BII. ELISA analysis showed that, compared with NM, DM led to significant increase of two representative advanced glycation end products (AGEs), namely CML (6.43 ± 0.76 ng/mg protein *vs*. 1.12 ± 0.24, $p < 0.05$, Fig. 8A) and pentosidine (16.43 ± 1.37 ng/mg protein *vs*. 4.12 ± 0.60, $p < 0.05$, Fig. 8B), as well as substantial increase of the receptor for AGEs (RAGE, Fig. 8D) in the VEC on titanium surface. Consistently, the CML in culture supernatant

was also increased by about 40 folds in DM (Fig. 8C). Immunohistochemical staining (Fig. 8E) showed that, compared with normal animals (NM), there was obvious increase of AGEs in the tissue around implants in diabetic animals (DM).

In DM, aminoguanidine (Ami), an inhibitor of the formation of AGEs [39], significantly reduced the levels of AGEs, both in VEC and in the supernatant, and the protein level of RAGE in VEC (Fig. 8). The soluble form of RAGE (sRAGE), a decoy receptor for AGEs, didn't make observable influence on the levels of AGEs, but induced significant reduction of RAGE in VEC. Both aminoguanidine and sRAGE inhibited the DM-induced up-regulation of NOX2 (Fig. 9C) and ROS (Fig. 9A and B; Fig. S3A) and improved the functions of mitochondria in VEC on titanium (Fig. 9D and E; Fig. S3B). These effects were accompanied by the alleviation of the DM-induced dysfunctions of VEC (Figs. 10), with the effects of sRAGE significantly better than those of aminoguanidine. The beneficial effects of sRAGE on VEC were further confirmed in vivo by the improved angiogenesis (Fig. 1), osteogenesis and osteointegration of implants (Fig. 2) in diabetic animals.

In NM, the existence of AGE (AGE-conjugated BSA) led to tremendous increase of RAGE in VEC (NM + AGE group *vs*. NM group), which level was even higher than that in DM, and significant augment of AGEs in VEC on material surface (Fig. 8). Furthermore, in NM, AGE also induced marked increase of NOX2 and ROS (Fig. 9A-C), mitochondrial dysfunction (Fig. 9D and E) and abnormal cell behaviors of

VEC (Figs. 10). However, all these AGE-induced abnormalities of VEC were effectively attenuated by sRAGE (NM + AGE + sRAGE group *vs*. NM + AGE group).

4. Discussion

Implant stability has been shown to be jeopardized by the delayed or impaired bone healing on bone-implant interface (BII) in diabetes patients with hyperglycemia. The mechanism underlying this phenomenon remains elusive, making it difficult to develop corresponding solutions through the innovation of implant materials. The main findings in this study are as follows (Fig. 11): (1) Diabetes led to VEC dysfunction and angiogenesis inhibition on BII, which contributed to the exiguity of osteoprogenitors and bone deposition on BII as well as the compromised osteointergration of implants. (2) Intracellular ROS overproduction and oxidative stress in VEC played a critical role in the diabetes-induced angiogenesis impairment at the interface; (3) The oxidative stress of VEC was triggered by the increased NOX expression and amplified by mitochondrial dysfunction which led to more ROS production from mitochondria. (4) Such metabolic disturbance of VEC was caused, at least partially, by the increase of AGEs on BII in diabetic milieu (DM).

In the bone repair on BII, angiogenesis in the metabolically active regenerating callus is required for supplying raw materials essential for tissue regeneration [9]. Diabetes, however, causes serious vascular complications which have been shown to be quite distinct among different organs and different vascular levels [12]. By now, the influences of diabetes on bone vasculature and their relationship with diabetic bone complications are still poorly understood [15]. In the present study, diabetic conditions led to significant dysfunction of VEC on titanium surface and poor blood

vessel formation on BII, which is in line with Peng et al. [40] showing the reduced angiogenesis and bone turnover in diabetic mice. Following the angiogenesis inhibition, osteoprogenitors on the BII became sparse (Fig. 1D), resulting in poor bone formation around implants and compromised implant osteointegration in diabetic animals (Fig. 2). This is consistent with Sojo et al. [41] demonstrating that angiogenesis occurs predominantly before the onset of osteogenesis and Fang et al. [42] showing that administration of anti-angiogenic drug prevents normal osteogenesis. The newly formed blood vessels ensure steady transport of circulating osteoprogenitor precursors to the healing sites [43]. In addition, the fact that osteogenesis is a vascular dependent process suggests that vascular endothelium itself serves as an indispensable regulator of cells involved in the healing process [43].

For a long time, endothelial cells that line capillaries were perceived just as passive conduits for blood. This stereotype, however, has been challenged by increasing evidence indicating the critical role of organ-specific VECs as an important regulator that sustain the homeostasis, metabolism and direct the regeneration of organs without provoking fibrosis [21]. These regulative functions of VEC are exerted in a perfusion-independent manner and by deploying sets of angiocrine factors, known as angiocrine functions [21]. For bone, Kusumbe et al. [38] have demonstrated that the bone vasculature contains specialized VECs that support bone maturation and regeneration by secreting angiocrine factors indispensable for osteogenesis, including Noggin and BMPs. The communication between osteoblastic cells and VEC ensures

the close spatial and temporal association of bone formation with vascularization, namely the coupling of angiogenesis and osteogenesis [38, 43, 44]. This coupling was reflected in our results by the selective distribution of osteoprogenitors near blood vessels (Fig. 1D) and the synchronism of the alteration tendencies of blood vessels, osteoprogenitors and new bone deposition on BII. In DM, the reduced gene expressions of Nog and Bmp-2 (Fig. 1F) following the angiogenesis impairment might reflect the decreased angiocrine function and account for the reduced activity of osteoprogenitors on BII. These together suggested that the diabetes-induced angiogenesis inhibition plays a critical role in the compromised implant osteointegration, which mechanism might also be implicated in the bone loss in diabetic patients with hyperglycemia. In addition, the experimental model used here might be applicable for studies on the angiogenesis on material-bone interface.

Surgical trauma arising from implantation induces a short-term oxidative stress which has been significantly connected to the inflammation and healing on BII and the fate of implanted biomaterials [18, 45]. Our previous study showed that the ROS overproduction on BII is a critical factor leading to the poor implant osteointegration in diabetes [20], while the detailed cellular mechanisms were not clearly identified. In the present study, obvious overproduction of ROS in VEC on titanium surface (Fig. 6A-C) and ROS-induced DNA damage in the tissue around implants (Fig. 6F) were observed under diabetic conditions. When intracellular ROS was inhibited from their two main sources, namely mitochondria and NOX, the diabetes-induced impairment

of VEC was significantly attenuated, with angiogenesis and bone regeneration on BII effectively improved. Our results are consistent with previous studies showing that oxidative stress of VEC is a key mechanism underlying many diabetic cardiovascular complications. These suggest that the diabetes-induced ROS accumulation is a key player in the VEC dysfunction and angiogenesis inhibition on BII [12, 13]. From another perspective, these propose vascular injury as a crucial mechanism underlying the pathological effects of ROS on BII.

Mitochondria and NOX are the two main sources of ROS in cells [22], while their exact roles in the diabetes-induced ROS overproduction on BII have not been clarified. Our previous work suggested that mitochondrial damage might be an important reason for the oxidative stress in osteoblasts on the BII in diabetes [23], which was not directly confirmed. In the present study, when the mitochondrial ROS were blocked by Mito-TEMPO, the DM-induced mitochondrial abnormalities as well as the oxidative stress and cell dysfunction of VEC were effectively ameliorated, indicating the role of mitochondria as an important contributor to the ROS overproduction in VEC on BII. NOX family are a major source of ROS in vasculature [46] and have been proposed to be key players in mediating the oxidative stress and endothelial dysfunction in diabetes [47, 48]. In our results, the effects of NOX inhibitor, apocynin (APO), revealed that the DM-induced increase of NOX is a critical reason for the ROS overproduction in VEC and the poor angiogenesis on BII. This is consistent with a recent report by Hema at al. [49] showing that the diabetes-induced oxidative stress

in osteoblast derives majorly from the up-regulation of NOX4. Remarkably, compared with Mito-TEMPO, APO led to more significant inhibition on the ROS (Fig. 6A-C), induced better cell behaviors of VEC in DM (Figs. 3-5), and also effectively attenuated the DM-induced mitochondrial dysfunction (Fig. 7). In fact, the excess ROS in cells could lead to irreversible damage to mitochondria, resulting in pathological production of mitochondrial ROS through the so-called ROS-induced ROS release [50, 51]. All these together suggest that the DM-induced ROS overproduction in VEC on BII might be triggered by the pathological increase of NOX, which causes mitochondrial dysfunction and much more ROS generation from mitochondria, amplifying the initial oxidative stress and cell damage. This "NOX-ROS-mitochondria-ROS" relationship in the VEC on BII needs further confirmation in studies in the future. Such ROS-overproducing mechanism might also be involved in the oxidative stress on material-tissue interface in many other diseased conditions, such as cardiovascular diseases [52], neurodegenerative diseases [53] and cancer [54, 55], making NOX a molecular therapeutic target for the modification of biomaterials to control the ROS generation on the interface.

As membrane proteins, NOX could generate ROS into both the intracellular and extracellular milieu (Fig. 11) [47]. Therefore, apart from cell damage, the DM-induced pathological activation of NOX might also dramatically increase the ROS concentration in the electrochemical micro-environment to which titanium surface is exposed. Although ROS production on BII is necessary for the thickening

of titanium oxide layer which adds to the stability and biocompatibility of titanium surface, high levels of ROS has been shown to accelerate Ti ion release from implant surface, pointing to ROS-induced corrosion [18]. In DM, there might be evidences of material corrosion and oxidative stress at/near the implant surface. These evidences, however, were not checked in our experiments, which is a limitation of the present study and necessitates further investigation on this issue in the future.

Advanced glycation end products (AGEs) are end products of non-enzymatic glycosylation reactions between reducing sugars and other biomolecules like proteins, lipids or nucleic acids [56]. They exist both inside and outside of cells, and influence cellular metabolism through receptor binding as well as intracellular signaling [39]. During aging and many diseases, such as neurodegenerative diseases, osteoarthritis and especially diabetes, the formation and deposition of AGEs greatly accelerate in many tissues, impacting extracellular and intracellular structure and function [39, 56]. Previous studies have shown that there is obvious increase of AGEs in bone in diabetes, which has been correlated to the much higher fracture risk in diabetic patients, although the underlying mechanism remains unclear [57-60]. AGEs have been identified as a substantial contributor to a variety of diabetic cardiovascular injuries including impaired retinal angiogenesis [56, 61]. However, the role of AGEs in the vascular abnormalities in diabetic bone has not been investigated.

In the present study, DM led to marked increase of both AGEs and the receptor for

AGEs (RAGE) in VEC on titanium as well as obvious increase of AGEs concentration in the bone tissue around implants (Fig. 8). The increased AGEs in bone could be in many kinds of cells, including VEC, and also in the extracellular matrix. As aforementioned, both the intracellular and the extracellular AGEs could influence cell metabolism. Given the vicious character of AGEs in many diseases, they have been the subject of ongoing research as an important therapeutic target through three main approaches: (1) preventing the formation of AGEs with drugs like aminoguanidine (Ami); (2) breaking crosslinks after they are formed and (3) preventing their negative effects through reducing RAGE or blocking the interaction between AGEs and RAGE with agents like sRAGE, a decoy receptor for AGEs [39, 56]. Our results showed that aminoguanidine partially attenuated the DM-induced abnormalities of VEC, while sRAGE induced better effects than aminoguanidine. In NM, AGE itself brought about obvious impairment of VEC on implants, which was effectively alleviated by sRAGE. Our results are consistent with previous reports demonstrating that an AGE–RAGE interaction promotes NOX activity, resulting in increased formation of ROS which conversely contributes to more formation of AGEs [39]. These together suggest that the increase of AGEs concentration on BII in diabetes is closely correlated to the metabolic stress and dysfunction of VEC, and the effects of AGEs were mediated mainly by RAGE. Besides, these also provide the oxidative stress-mediated vascular injury as a new mechanism underlying the pathological role of AGEs in diabetic osteopathy. Furthermore, it has been indicated that cross-linking in the organic bone matrix by AGEs adversely affects the quality

and mechanical properties of bone material [57, 58], which might influence the mechanical interlocking between bone and implants. Therefore, developing new implant materials, which could inhibit the formation, deposition or pathological effects of AGEs on BII, might be a promising strategy to accelerate osteointegration of implant materials in many disease conditions, especially diabetes.

The performance of a biomaterial is usually considered to be an intrinsic property of the material, with little attention paid to the role of host tissue [62]. This "one material fits all" mindset ignores profound differences in target tissues that affect their responses to materials [63]. Actually, it has been challenged by increasing clinical evidence showing that the performance of biomaterials show marked difference under healthy and diseased conditions [16]. Thus, it has been proposed that the biocompatibility rules are in need of rethinking and it is necessary to take the substantial effects of diseases on tissue/biomaterial interactions into consideration [62]. A better understanding of events at the tissue-material interface in specific diseased conditions is needed, which could provide new vistas for material research and therapeutic potential. The integration with target tissues is crucial for most implant biomaterials [16, 17]. In the present study, our results suggested the "AGEs-NOX-oxidative stress-angiogenesis impairment-poor osteogenesis" logical axis as critical mechanisms underlying the diabetes-induced poor osteointegration of titanium implants. These mechanisms might also be implicated in the compromised implant integration in patients suffering from diseases other than diabetes. Of course,

however, other diseases and materials might display determinant factors different from those of titanium in diabetes. For example, the elevated concentration of ROS in the tumor environment might lead to faster degradation of materials that undergo oxidative degradation [18]. And, the enzyme concentrations in an inflammatory environment could influence the materials that undergo enzymatic degradation [63, 64].

In the development of novel implant biomaterials in the future, two strategies could be utilized to target NOX or AGEs to attenuate the redundant ROS production on BII: (1) We can evaluate the effects of various biomaterials on NOX and AGEs to find some materials capable of inhibiting the production or pathological effects of NOX or AGEs. Next, some of these materials could be used, as basic or additional components, to fabricate novel functionalized implants with better osteointegration; (2) We can integrate some certain bioactive factors in implant materials to specifically interfere with the two pathological accessaries on BII. These bioactive agents could be specific inhibiting drugs, like apocynin (APO) and sRAGE, or shRNA (for gene silencing) which could down-regulate the expressions of NOX, RAGE or other key molecules mediating the formation or cell signaling of AGEs. Of course, these two strategies could be combined together to modulate the oxidative stress on BII and advance the bone regeneration and osteointegration of implanted materials. These might help to improve the performance of biomaterials in diseased tissues which could induce excessive oxidative stress in tissue/material interactions. The related diseases include

metabolic diseases like diabetes [65], neurodegenerative diseases like Parkinson's disease [66], inflammatory diseases like osteoarthritis [67], many kinds of cancer [68] and so on.

5. Conclusions

The present study demonstrated that the diabetes-induced increase of AGEs in the bone tissue around implants causes intracellular ROS overproduction and oxidative stress of VEC, which result in dysfunction of VEC and impaired angiogenesis on bone-implant interface (BII). This angiogenesis impairment plays a critical role in the poor osteogenesis on BII and the compromised osteointegration of titanium implants. The ROS overproduction in VEC was triggered by the increase of NADPH oxidases (NOX), which leads to mitochondrial dysfunction and more ROS generation from mitochondria. Bioactive agents targeting at NOX or AGEs could effectively mitigate the diabetes-induced metabolic stress of VEC on BII, thus promote the angiogenesis and the osteointegration of implants. Our findings provide deeper insights into the mechanisms underlying diabetes-induced poor bone repair and implant failure targeting at the BII, suggesting key therapeutic targets for corresponding solutions in the future. Developing new implant materials, which could inhibit the increase and/or effects of NOX or AGEs on BII, might be an efficacious strategy to promote the angiogenesis and osteointegration of endosseous implants and reduce the implant failure in diabetic patients with hyperglycemia.

Acknowledgements

This work was supported by the Research Fund for the National Natural Science Foundation of China to Ya-Fei Feng (No. 81401769), to Lin Wang (No. 81371933) and to Wei Lei (No. 81672132).

References

[1] Tobin EJ. Recent coating developments for combination devices in orthopedic and dental applications: A literature review. Adv Drug Deliv Rev 112 (2017) 88-100.

[2] Raphel J, Holodniy M, Goodman SB, Heilshorn SC. Multifunctional coatings to simultaneously promote osseointegration and prevent infection of orthopaedic implants. Biomaterials 84 (2016) 301-314.

[3] Oates TW, Huynh-Ba G, Vargas A, Alexander P, Feine J. A critical review of diabetes, glycemic control, and dental implant therapy. Clin Oral Implants Res 24 (2013) 117-127.

[4] Chrcanovic BR, Albrektsson T, Wennerberg A. Diabetes and oral implant failure: a systematic review. J Dent Res 93 (2014) 859-867.

[5] Annibali S, Pranno N, Cristalli MP, La Monaca G, Polimeni A. Survival Analysis of Implant in Patients With Diabetes Mellitus: A Systematic Review. Implant Dent 25 (2016) 663-674.

[6] Le NN, Rose MB, Levinson H, Klitzman B. Implant healing in experimental animal models of diabetes. J Diabetes Sci Technol 5 (2011) 605-618.

[7] Moraschini V, Barboza ES, Peixoto GA. The impact of diabetes on dental implant failure: a systematic review and meta-analysis. Int J Oral Maxillofac Surg 45 (2016) 1237-1245.

[8] International Diabetes Federation. IDF Diabetes Atlas, 8th edn. Brussels, Belgium: International Diabetes Federation, 2017. http://www.diabetesatlas.org.

[9] Stegen S, van Gastel N, Carmeliet G. Bringing new life to damaged bone: the importance of angiogenesis in bone repair and regeneration. Bone 70 (2015) 19-27.

[10] Quinlan E, Partap S, Azevedo MM, Jell G, Stevens MM, O'Brien FJ. Hypoxia-mimicking bioactive glass/collagen glycosaminoglycan composite scaffolds to enhance angiogenesis and bone repair. Biomaterials 52 (2015) 358-366.

[11] Sivaraj KK, Adams RH. Blood vessel formation and function in bone. Development 143 (2016) 2706-2715.

[12] Beckman JA, Creager MA. Vascular Complications of Diabetes. Circ Res 118 (2016) 1771-1785.

[13] Sena CM, Pereira AM, Seica R. Endothelial dysfunction - a major mediator of diabetic vascular disease. Biochim Biophys Acta 1832 (2013) 2216-2231.

[14] Fajardo RJ. Is Diabetic Skeletal Fragility Associated with Microvascular Complications in Bone? Curr Osteoporos Rep 15 (2017) 1-8.

[15] Shanbhogue VV, Hansen S, Frost M, Brixen K, Hermann AP. Bone disease in diabetes: another manifestation of microvascular disease? Lancet Diabetes Endocrinol 5 (2017) 827-838.

[16] Haiat G, Wang HL, Brunski J. Effects of biomechanical properties of the bone-implant interface on

dental implant stability: from in silico approaches to the patient's mouth. Annu Rev Biomed Eng 16 (2014) 187-213.

[17] Puleo DA, Nanci A. Understanding and controlling the bone-implant interface. Biomaterials 20 (1999) 2311-2321.

[18] Mouthuy PA, Snelling SJB, Dakin SG, Milkovic L, Gasparovic AC, Carr AJ, Zarkovic N. Biocompatibility of implantable materials: An oxidative stress viewpoint. Biomaterials 109 (2016) 55-68.

[19] Bryan N, Ahswin H, Smart N, Bayon Y, Wohlert S, Hunt JA. Reactive oxygen species (ROS)--a family of fate deciding molecules pivotal in constructive inflammation and wound healing. Eur Cell Mater 24 (2012) 249-265.

[20] Feng YF, Wang L, Zhang Y, Li X, Ma ZS, Zou JW, Lei W, Zhang ZY. Effect of reactive oxygen species overproduction on osteogenesis of porous titanium implant in the present of diabetes mellitus. Biomaterials 34 (2013) 2234-2243.

[21] Rafii S, Butler JM, Ding BS. Angiocrine functions of organ-specific endothelial cells. Nature 529 (2016) 316-325.

[22] Giacco F, Brownlee M. Oxidative stress and diabetic complications. Circ Res 107 (2010) 1058-1070.

[23] Hu XF, Wang L, Lu YZ, Xiang G, Wu ZX, Yan YB, Zhang Y, Zhao X, Zang Y, Shi L, Lei W, Feng YF. Adiponectin improves the osteointegration of titanium implant under diabetic conditions by reversing mitochondrial dysfunction via the AMPK pathway in vivo and in vitro. Acta Biomater 61 (2017) 233-248.

[24] Rouxel O, Da Silva J, Beaudoin L, Nel I, Tard C, Cagninacci L, Kiaf B, Oshima M, Diedisheim M, Salou M, Corbett A, Rossjohn J, McCluskey J, Scharfmann R, Battaglia M, Polak M, Lantz O, Beltrand J, Lehuen A. Cytotoxic and regulatory roles of mucosal-associated invariant T cells in type 1 diabetes. Nat Immunol 18 (2017) 1321-1331.

[25] Moverare-Skrtic S, Henning P, Liu X, Nagano K, Saito H, Borjesson AE, Sjogren K, Windahl SH, Farman H, Kindlund B, Engdahl C, Koskela A, Zhang FP, Eriksson EE, Zaman F, Hammarstedt A, Isaksson H, Bally M, Kassem A, Lindholm C, Sandberg O, Aspenberg P, Savendahl L, Feng JQ, Tuckermann J, Tuukkanen J, Poutanen M, Baron R, Lerner UH, Gori F, Ohlsson C. Osteoblast-derived WNT16 represses osteoclastogenesis and prevents cortical bone fragility fractures. Nat Med 20 (2014) 1279-1288.

[26] Ma QL, Zhao LZ, Liu RR, Jin BQ, Song W, Wang Y, Zhang YS, Chen LH, Zhang YM. Improved implant osseointegration of a nanostructured titanium surface via mediation of macrophage polarization. Biomaterials 35 (2014) 9853-9867.

[27] Kelly NH, Schimenti JC, Patrick Ross F, van der Meulen MC. A method for isolating high quality RNA from mouse cortical and cancellous bone. Bone 68 (2014) 1-5.

[28] Tong X, Kono T, Anderson-Baucum EK, Yamamoto W, Gilon P, Lebeche D, Day RN, Shull GE, Evans-Molina C. SERCA2 Deficiency Impairs Pancreatic beta-Cell Function in Response to Diet-Induced Obesity. Diabetes 65 (2016) 3039-3052.

[29] Setyawati MI, Tay CY, Chia SL, Goh SL, Fang W, Neo MJ, Chong HC, Tan SM, Loo SC, Ng KW, Xie JP, Ong CN, Tan NS, Leong DT. Titanium dioxide nanomaterials cause endothelial cell leakiness by disrupting the homophilic interaction of VE-cadherin. Nat Commun 4 (2013) 1673.

[30] Hassman LM, Ellison TJ, Kedes DH. KSHV infects a subset of human tonsillar B cells, driving proliferation and plasmablast differentiation. J Clin Invest 121 (2011) 752-768.

[31] Outeda P, Huso DL, Fisher SA, Halushka MK, Kim H, Qian F, Germino GG, Watnick T. Polycystin

signaling is required for directed endothelial cell migration and lymphatic development. Cell Rep 7 (2014) 634-644.

[32] Pin AL, Houle F, Fournier P, Guillonneau M, Paquet ER, Simard MJ, Royal I, Huot J. Annexin-1-mediated endothelial cell migration and angiogenesis are regulated by vascular endothelial growth factor (VEGF)-induced inhibition of miR-196a expression. J Biol Chem 287 (2012) 30541-30551.

[33] Puntel RL, Nogueira CW, Rocha JB. Krebs cycle intermediates modulate thiobarbituric acid reactive species (TBARS) production in rat brain in vitro. Neurochem Res 30 (2005) 225-235.

[34] Dubois A, Ginet C, Furstoss N, Belaid A, Hamouda MA, El Manaa W, Cluzeau T, Marchetti S, Ricci JE, Jacquel A, Luciano F, Driowya M, Benhida R, Auberger P, Robert G. Differentiation inducing factor 3 mediates its anti-leukemic effect through ROS-dependent DRP1-mediated mitochondrial fission and induction of caspase-independent cell death. Oncotarget 7 (2016) 26120-26136.

[35] Landshamer S, Hoehn M, Barth N, Duvezin-Caubet S, Schwake G, Tobaben S, Kazhdan I, Becattini B, Zahler S, Vollmar A, Pellecchia M, Reichert A, Plesnila N, Wagner E, Culmsee C. Bid-induced release of AIF from mitochondria causes immediate neuronal cell death. Cell Death Differ 15 (2008) 1553-1563.

[36] Moriyama T, Kemi M, Okumura C, Yoshihara K, Horie T. Involvement of advanced glycation end-products, pentosidine and N(epsilon)-(carboxymethyl)lysine, in doxorubicin-induced cardiomyopathy in rats. Toxicology 268 (2010) 89-97.

[37] San Martin A, Foncea R, Laurindo FR, Ebensperger R, Griendling KK, Leighton F. Nox1-based NADPH oxidase-derived superoxide is required for VSMC activation by advanced glycation end-products. Free Radic Biol Med 42 (2007) 1671-1679.

[38] Kusumbe AP, Ramasamy SK, Adams RH. Coupling of angiogenesis and osteogenesis by a specific vessel subtype in bone. Nature 507 (2014) 323-328.

[39] Ott C, Jacobs K, Haucke E, Navarrete Santos A, Grune T, Simm A. Role of advanced glycation end products in cellular signaling. Redox Biol 2 (2014) 411-429.

[40] Peng J, Hui K, Hao C, Peng Z, Gao QX, Jin Q, Lei G, Min J, Qi Z, Bo C, Dong QN, Bing ZH, Jia XY, Fu DL. Low bone turnover and reduced angiogenesis in streptozotocin-induced osteoporotic mice. Connect Tissue Res 57 (2016) 277-289.

[41] Sojo K, Sawaki Y, Hattori H, Mizutani H, Ueda M. Immunohistochemical study of vascular endothelial growth factor (VEGF) and bone morphogenetic protein-2, -4 (BMP-2, -4) on lengthened rat femurs. J Craniomaxillofac Surg 33 (2005) 238-245.

[42] Fang TD, Salim A, Xia W, Nacamuli RP, Guccione S, Song HM, Carano RA, Filvaroff EH, Bednarski MD, Giaccia AJ, Longaker MT. Angiogenesis is required for successful bone induction during distraction osteogenesis. J Bone Miner Res 20 (2005) 1114-1124.

[43] Saran U, Gemini Piperni S, Chatterjee S. Role of angiogenesis in bone repair. Arch Biochem Biophys 561 (2014) 109-117.

[44] Raftery RM, Mencia Castano I, Chen G, Cavanagh B, Quinn B, Curtin CM, Cryan SA, O'Brien FJ. Translating the role of osteogenic-angiogenic coupling in bone formation: Highly efficient chitosan-pDNA activated scaffolds can accelerate bone regeneration in critical-sized bone defects. Biomaterials 149 (2017) 116-127.

[45] Dohan Ehrenfest DM, Coelho PG, Kang BS, Sul YT, Albrektsson T. Classification of osseointegrated implant surfaces: materials, chemistry and topography. Trends Biotechnol 28 (2010) 198-206.

[46] Sahoo S, Meijles DN, Pagano PJ. NADPH oxidases: key modulators in aging and age-related cardiovascular diseases? Clin Sci (Lond) 130 (2016) 317-335.

[47] Drummond GR, Selemidis S, Griendling KK, Sobey CG. Combating oxidative stress in vascular disease: NADPH oxidases as therapeutic targets. Nat Rev Drug Discov 10 (2011) 453-471.
[48] Gorin Y, Block K. Nox as a target for diabetic complications. Clin Sci (Lond) 125 (2013) 361-382.
[49] Kalyanaraman H, Schwaerzer G, Ramdani G, Castillo F, Scott BT, Dillmann W, Sah RL, Casteel DE, Pilz RB. Potein Kinase G Activation Reverses Oxidative Stress and Restores Osteoblast Function and Bone Formation in Male Mice With Type 1 Diabetes. Diabetes (2018).
[50] Zorov DB, Juhaszova M, Sollott SJ. Mitochondrial reactive oxygen species (ROS) and ROS-induced ROS release. Physiol Rev 94 (2014) 909-950.
[51] Murphy E, Ardehali H, Balaban RS, DiLisa F, Dorn GW, 2nd, Kitsis RN, Otsu K, Ping P, Rizzuto R, Sack MN, Wallace D, Youle RJ, American Heart Association Council on Basic Cardiovascular Sciences CoCC, Council on Functional G, Translational B. Mitochondrial Function, Biology, and Role in Disease: A Scientific Statement From the American Heart Association. Circ Res 118 (2016) 1960-1991.
[52] Garcia-Redondo AB, Aguado A, Briones AM, Salaices M. NADPH oxidases and vascular remodeling in cardiovascular diseases. Pharmacol Res 114 (2016) 110-120.
[53] Ma MW, Wang J, Zhang Q, Wang R, Dhandapani KM, Vadlamudi RK, Brann DW. NADPH oxidase in brain injury and neurodegenerative disorders. Mol Neurodegener 12 (2017) 7.
[54] Bonner MY, Arbiser JL. Targeting NADPH oxidases for the treatment of cancer and inflammation. Cell Mol Life Sci 69 (2012) 2435-2442.
[55] Roy K, Wu Y, Meitzler JL, Juhasz A, Liu H, Jiang G, Lu J, Antony S, Doroshow JH. NADPH oxidases and cancer. Clin Sci (Lond) 128 (2015) 863-875.
[56] Goldin A, Beckman JA, Schmidt AM, Creager MA. Advanced glycation end products: sparking the development of diabetic vascular injury. Circulation 114 (2006) 597-605.
[57] Napoli N, Chandran M, Pierroz DD, Abrahamsen B, Schwartz AV, Ferrari SL, Bone IOF, Diabetes Working G. Mechanisms of diabetes mellitus-induced bone fragility. Nat Rev Endocrinol (2016).
[58] Yamamoto M, Sugimoto T. Advanced Glycation End Products, Diabetes, and Bone Strength. Curr Osteoporos Rep 14 (2016) 320-326.
[59] Karim L, Bouxsein ML. Effect of type 2 diabetes-related non-enzymatic glycation on bone biomechanical properties. Bone 82 (2016) 21-27.
[60] Ganeko K, Masaki C, Shibata Y, Mukaibo T, Kondo Y, Nakamoto T, Miyazaki T, Hosokawa R. Bone Aging by Advanced Glycation End Products: A Multiscale Mechanical Analysis. J Dent Res 94 (2015) 1684-1690.
[61] Stitt AW, McGoldrick C, Rice-McCaldin A, McCance DR, Glenn JV, Hsu DK, Liu FT, Thorpe SR, Gardiner TA. Impaired retinal angiogenesis in diabetes: role of advanced glycation end products and galectin-3. Diabetes 54 (2005) 785-794.
[62] Ratner BD. Healing with medical implants: The body battles back. Sci Transl Med 7 (2015) 272fs274.
[63] Oliva N, Carcole M, Beckerman M, Seliktar S, Hayward A, Stanley J, Parry NM, Edelman ER, Artzi N. Regulation of dendrimer/dextran material performance by altered tissue microenvironment in inflammation and neoplasia. Sci Transl Med 7 (2015) 272ra211.
[64] Selders GS, Fetz AE, Radic MZ, Bowlin GL. An overview of the role of neutrophils in innate immunity, inflammation and host-biomaterial integration. Regen Biomater 4 (2017) 55-68.
[65] Rochette L, Zeller M, Cottin Y, Vergely C. Diabetes, oxidative stress and therapeutic strategies. Biochim Biophys Acta 1840 (2014) 2709-2729.
[66] Jiang T, Sun Q, Chen S. Oxidative stress: A major pathogenesis and potential therapeutic target of

antioxidative agents in Parkinson's disease and Alzheimer's disease. Prog Neurobiol 147 (2016) 1-19.

[67] Lepetsos P, Papavassiliou AG. ROS/oxidative stress signaling in osteoarthritis. Biochim Biophys Acta 1862 (2016) 576-591.

[68] Poprac P, Jomova K, Simunkova M, Kollar V, Rhodes CJ, Valko M. Targeting Free Radicals in Oxidative Stress-Related Human Diseases. Trends Pharmacol Sci 38 (2017) 592-607.

Captions

Figure 1. The angiogenesis and osteoprogenitors on bone-implant interface (BII) 14 days after implantation. (A) Immunofluorescent staining of EMCN, a marker of endothelial cells, shows the blood vessels in the bone tissue around titanium screw. White dashed lines label the approximate border lines between the tissue and the screw threads. Yellow dashed lines label the outer boundary of the region of interest (ROI, Fig. 2E). Scale bar: 50 μm. (B) Histomorphometric measurement of the area ratio of blood vessels in the ROI on BII. For methodological details, please see Fig. S1. (C) qPCR analysis of the mRNA level of EMCN in the tissue around implants. (D) Images of osteoprogenitors labeled by osterix (OSX) on BII show their distribution adjacent to blood vessels. The last row shows the tissue ingrowth into a backlash of screw threads. Scale bar: 40 μm in the above and 20 μm in the below. (E) The number of OSX+ cells in the ROI around implants. qPCR analysis of the mRNA expressions of three indispensable cytokines for intercellular communication between VEC and osteoblastic cells (F) as well as two key genes in osteoprogenitors for osteogenic differentiation (G). APO, apocynin, an inhibitor of NADPH oxidases (NOX); sRAGE, the soluble form of receptor for advanced glycation end products (AGEs), a decoy receptor for AGEs. $*p < 0.05$ *vs*. NM group; $^{\#}p < 0.05$ *vs*. DM group.

Figure 2. New bone formation on BII. (A) Fluorescent images of histological sections showing temporal fluorochrome labeled new mineral deposition by calcein (green, at 2 weeks) and alizarin complexone (red, at 4 weeks). (B) The ratio of bone

formation area to the total area of ROI (BFA/TA) in fluorochrome analysis. (C) The ratio of bone volume to total volume (BV/TV) in the ROI around implants. 3D-reconstructed (D) and 2D cross-section (E) images in micro-CT analysis show the in vivo model and the ROI (yellow). (F) The newly formed bone (yellow) around implants (white). Scale bar: 50 μm in (A) and 300 μm in (D-F). APO, apocynin; sRAGE, the soluble form of receptor for AGEs. *$p < 0.05$ *vs*. NM group; $^{\#}p < 0.05$ *vs*. DM group.

Figure 3. The adhesion and morphology of VEC on titanium alloy surface after 3 days of incubation. (A) Fluorescent images of the cytoskeleton (red) and vinculin (green, a protein in focal adhesion plaques) show the cell adhesion and morphology. The actin filaments (red) of VEC were stained with Rhodamine-phalloidin and cell nuclei (blue) were stained with DAPI. Arrowheads indicate the twisted cytoskeleton and arrows indicate the intracellular vacuoles. The image in white box is an enlarged view of three cells with twisted cytoskeleton. Scale bar: 50 μm in the above and 20 μm in the below. (B) SEM images of VEC on titanium surface. Scale bar: 10 μm. Mito, Mito-TEMPO, a mitochondria-targeted ROS antagonist; APO, apocynin.

Figure 4. The proliferation of VEC on titanium surface after 3 days of incubation. (A) Fluorescent images show the cell proliferation marker, Ki-67 (red), in VEC. (B) Enlarged view of the corresponding white boxes in (A) show the expression and distribution of Ki-67 in a VEC during mitosis on implant surface. Proliferation of

VEC was quantified by cell density (C), the percentage of Ki67+ cells (D) and colorimetric MTT assay (E). Scale bar: 20 μm in (A) and 5 μm in (B). Mito, Mito-TEMPO; APO, apocynin. *$p < 0.05$ *vs*. NM group; $^{\#}p < 0.05$ *vs*. DM group.

Figure 5. Angiogenesis in vitro and cell migration of VEC after incubation for 7 days. (A) Representative images in tube formation assay show the angiogenesis in vitro. Blue plus signs label the branch points of tubes. Quantitative analysis of cumulative tube length (B) and branch points (C) per microscopic field. (D) Quantification of cell migration with the number of migrated cells in the wounds at 12 h. (E) Representative images from wound-healing assay show the migration of VEC. Confluent monolayers were photographed at 0 h and 12 h after wounding. Dashed lines indicate the borders of the wound at 0 h. Scale bar: 50 μm in (A) and 200 μm in (E). Mito, Mito-TEMPO; APO, apocynin. *$p < 0.05$ *vs*. NM group; $^{\#}p < 0.05$ *vs*. DM group.

Figure 6. The levels of oxidative stress in the VEC on implants in vitro and in the tissue on BII. (A) Images of DCF fluorescence showing the general ROS level in cells. Scale bar: 100 μm in the above and 20 μm in the below. (B) Quantitative analysis of intracellular ROS level with the relative DCF fluorescence intensity measured by flow cytometry. (C) MDA level accessed for intracellular lipid peroxidation. (D) The numbers of cells positive for 8-OHdG (a marker of DNA damage caused by oxidative stress) in the ROI on the interface. (E) Western blot

analysis of the protein level of NOX2 in VEC on titanium surface. (F) Immunohistochemical images of 8-OHdG in the tissue around implants. Scale bar: 50 μm. Mito, Mito-TEMPO; APO, apocynin. *$p < 0.05$ *vs*. NM group; $^{\#}p < 0.05$ *vs*. DM group.

Figure 7. The mitochondrial function in VEC on titanium surface after 7 days of incubation. (A) ATP production level in VEC measured by a luminescence ATP detection assay. (B) Mitochondrial membrane potential (MMP) determined by the red/green ratio in JC-1 staining. (C) Typical images of JC-1 staining showing the MMP in different groups. JC-1 is a cationic dye that exhibits potential-dependent accumulation in mitochondria, indicated by a fluorescence emission shift from green to red. Mitochondrial depolarization is reflected by a decrease in the red/green fluorescence ratio. Scale bar: 20 μm. Mito, Mito-TEMPO; APO, apocynin. *$p < 0.05$ *vs*. NM group; $^{\#}p < 0.05$ *vs*. DM group.

Figure 8. The levels of advanced glycation end products (AGEs) and receptor for AGE (RAGE) in VEC on implants, in culture supernatant and in tissue around implants. The levels of two representative AGEs, N^{ε}-carboxymethyllysine (CML, A) and pentosidine (B), in VEC as well as the level of CML in supernatant (C) were determined by ELISA assay after 7 days of incubation. (D) The protein expression of RAGE in VEC was assessed by western blot analysis. (E) Immunohistochemical images of AGEs in the tissue around implants 14 days after implantation. Scale bar:

50 μm. AGE, AGE-conjugated BSA; Ami, aminoguanidine, an inhibitor of AGEs formation. *$p < 0.05$ *vs*. NM group; $^{\#}p < 0.05$ *vs*. DM group; $^{\&}p < 0.05$ *vs*. NM+AGE group.

Figure 9. The oxidative stress levels and mitochondrial function in VEC on titanium under different conditions. (A) Images of DCF fluorescence showing the general ROS level in cells. (B) Quantitative analysis of intracellular ROS level with the relative DCF fluorescence intensity measured by flow cytometry. (C) Western blot analysis of the protein level of NOX2 in VEC. (D) Mitochondrial membrane potential (MMP) determined by the red/green ratio in JC-1 staining. (E) Typical images of JC-1 staining showing the MMP of VEC in different groups. Scale bar: 20 μm in (A) and 25 μm in (E). Ami, aminoguanidine. *$p < 0.05$ *vs*. NM group; $^{\#}p < 0.05$ *vs*. DM group; $^{\&}p < 0.05$ *vs*. NM+AGE group.

Figure 10. The biological functions of VEC on titanium after 7 days of incubation under different conditions. (A) Fluorescent images of the cytoskeleton (red) and vinculin (green) show the cell adhesion and morphology on implant surface. The actin filaments (red) were stained with Rhodamine-phalloidin and cell nuclei (blue) were stained with DAPI. Scale bar: 25 μm. (B) Representative images in tube formation assay show the angiogenesis in vitro. Blue plus signs label the branch points of tubes. (C) Quantitative analysis of the angiogenesis by cumulative tube length per field. (D) Proliferation of VEC was quantified by colorimetric MTT assay. (F) Representative

images from wound-healing assay show the migration of VEC. Confluent monolayers were photographed at 0 h and 12 h after wounding. Dashed lines indicate the border of the wound at 0 h. (E) Quantification of cell migration with the number of migrated cells in the wounds at 12 h. Scale bar: 20 μm in (A), 50 μm in (B); 200 μm in (F). Ami, aminoguanidine. $^{*}p < 0.05$ *vs*. NM group; $^{\#}p < 0.05$ *vs*. DM group; $^{\&}p < 0.05$ *vs*. NM+AGE group.

Figure 11. Schematic diagram summarizing the main findings in this article. For explanation, please see the first paragraph in the discussion section.

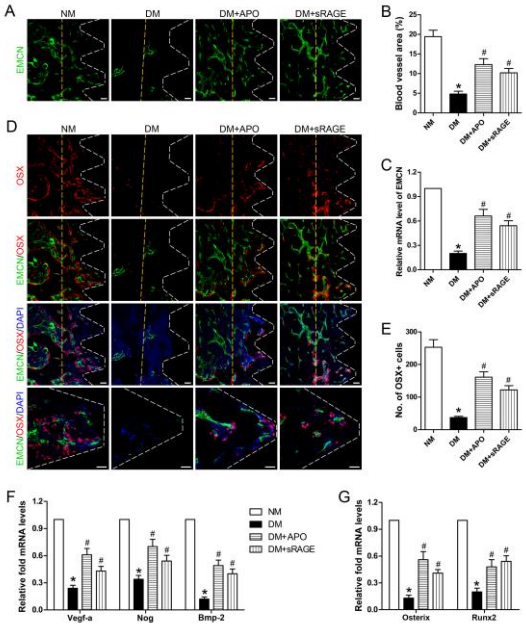

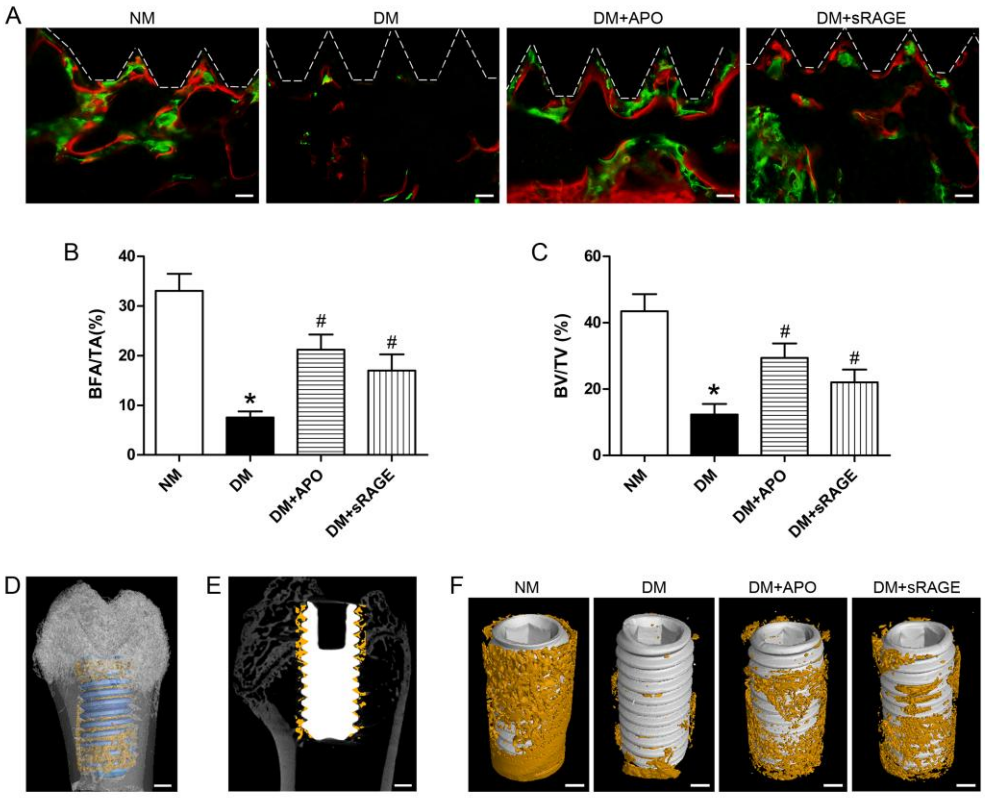

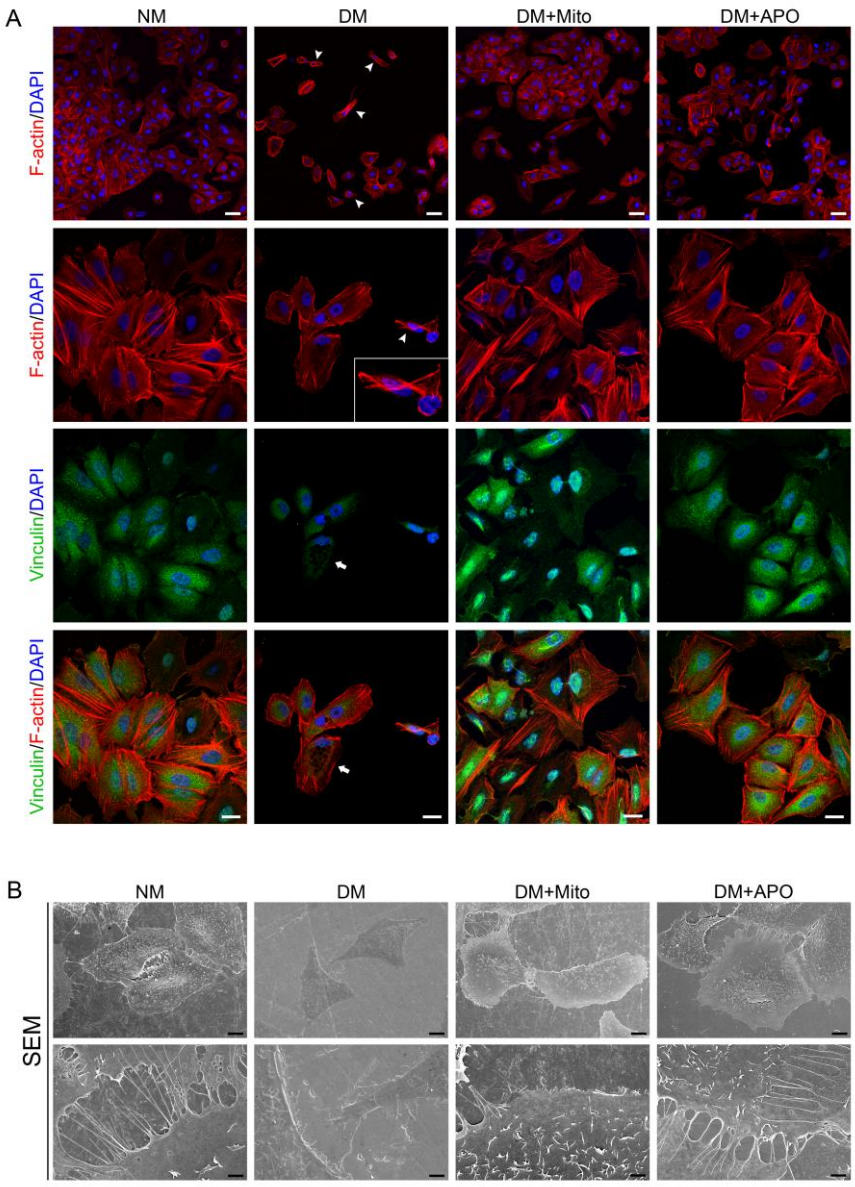

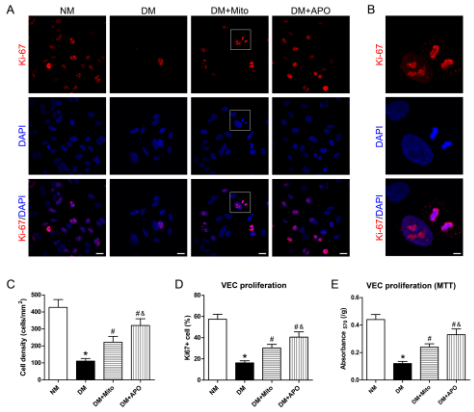

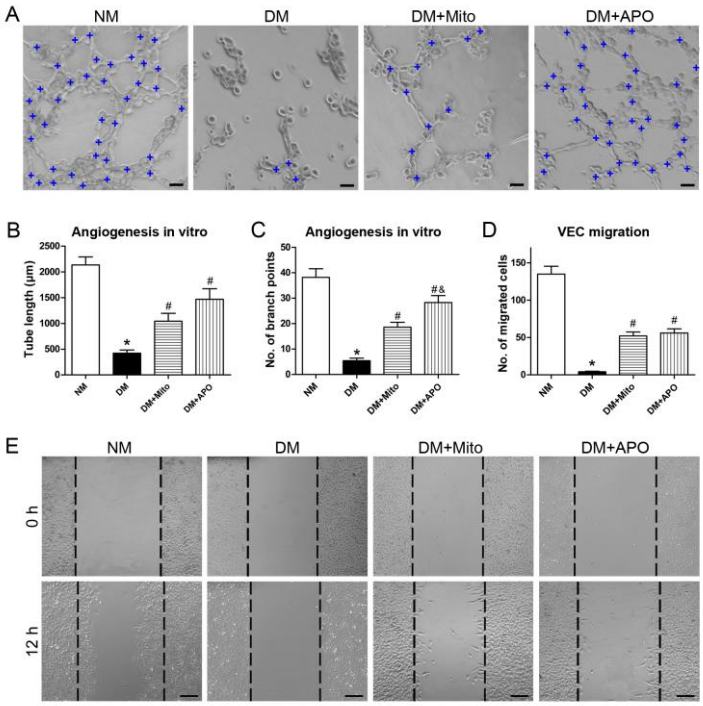

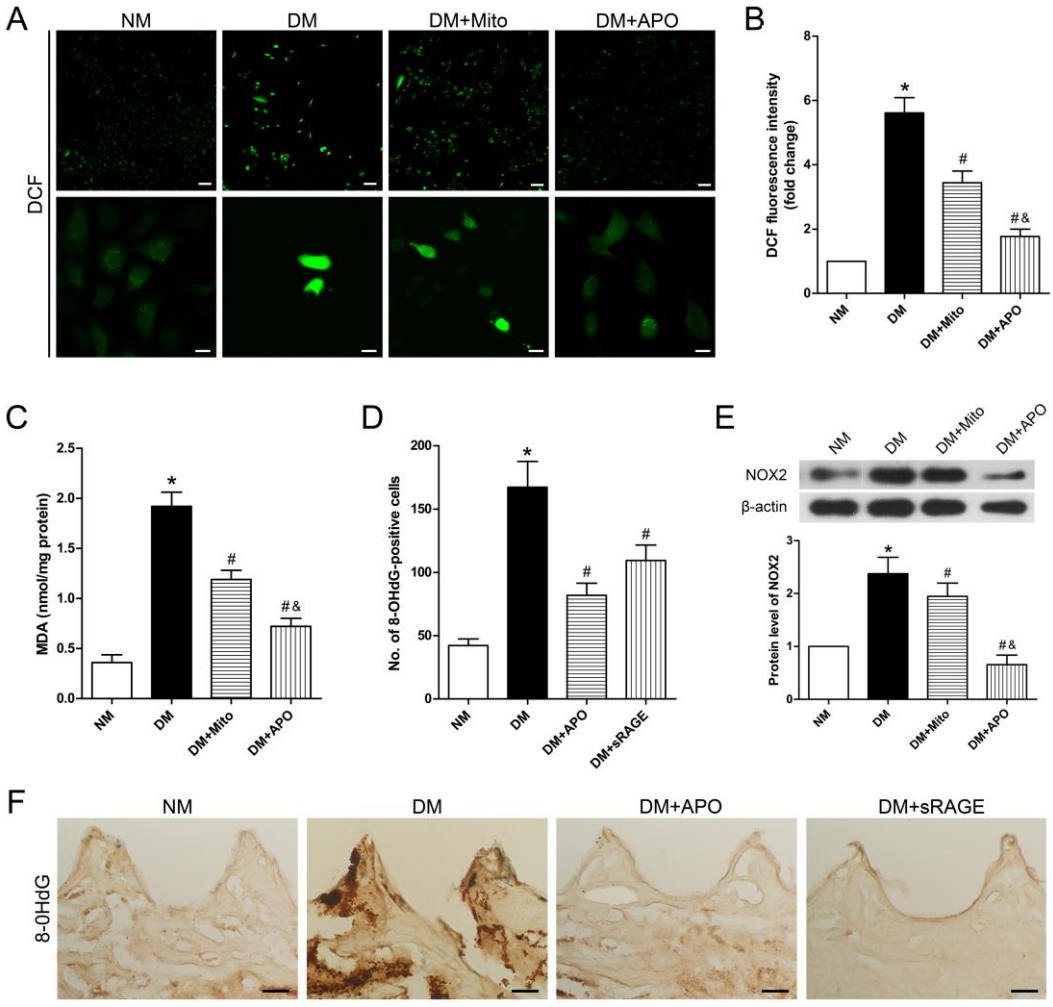

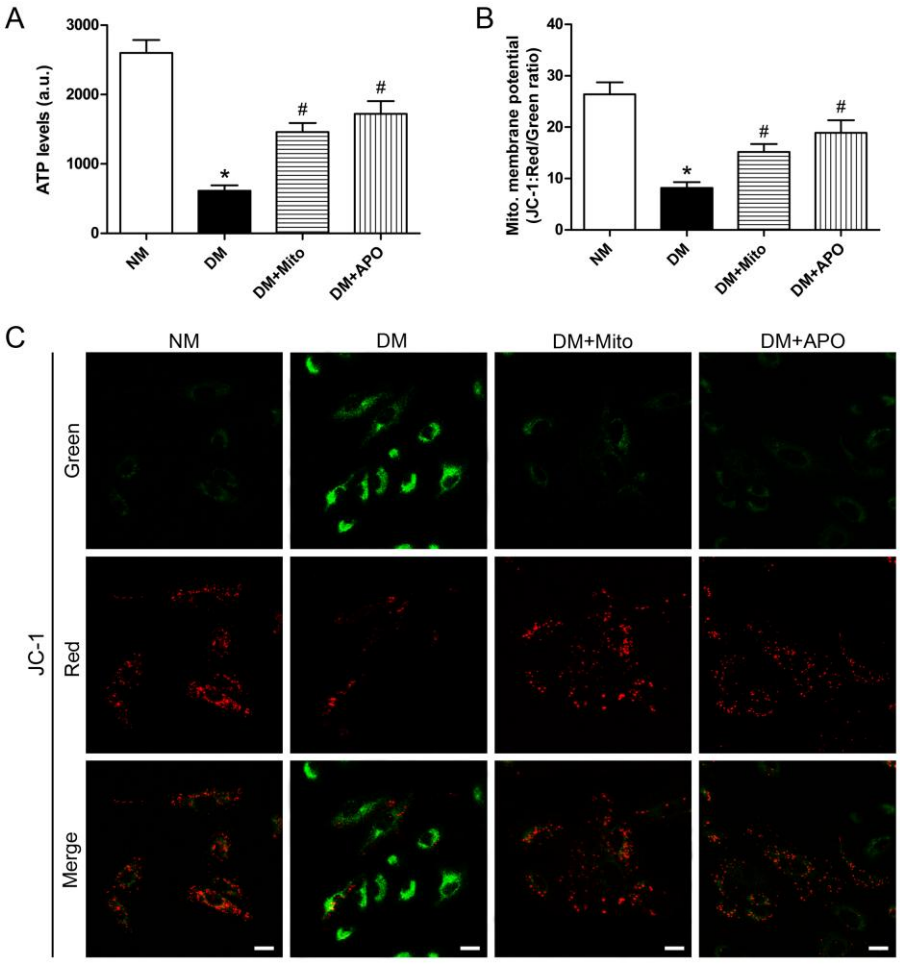

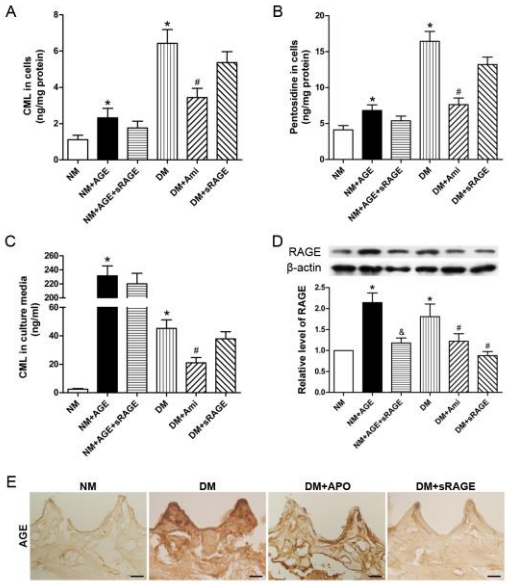

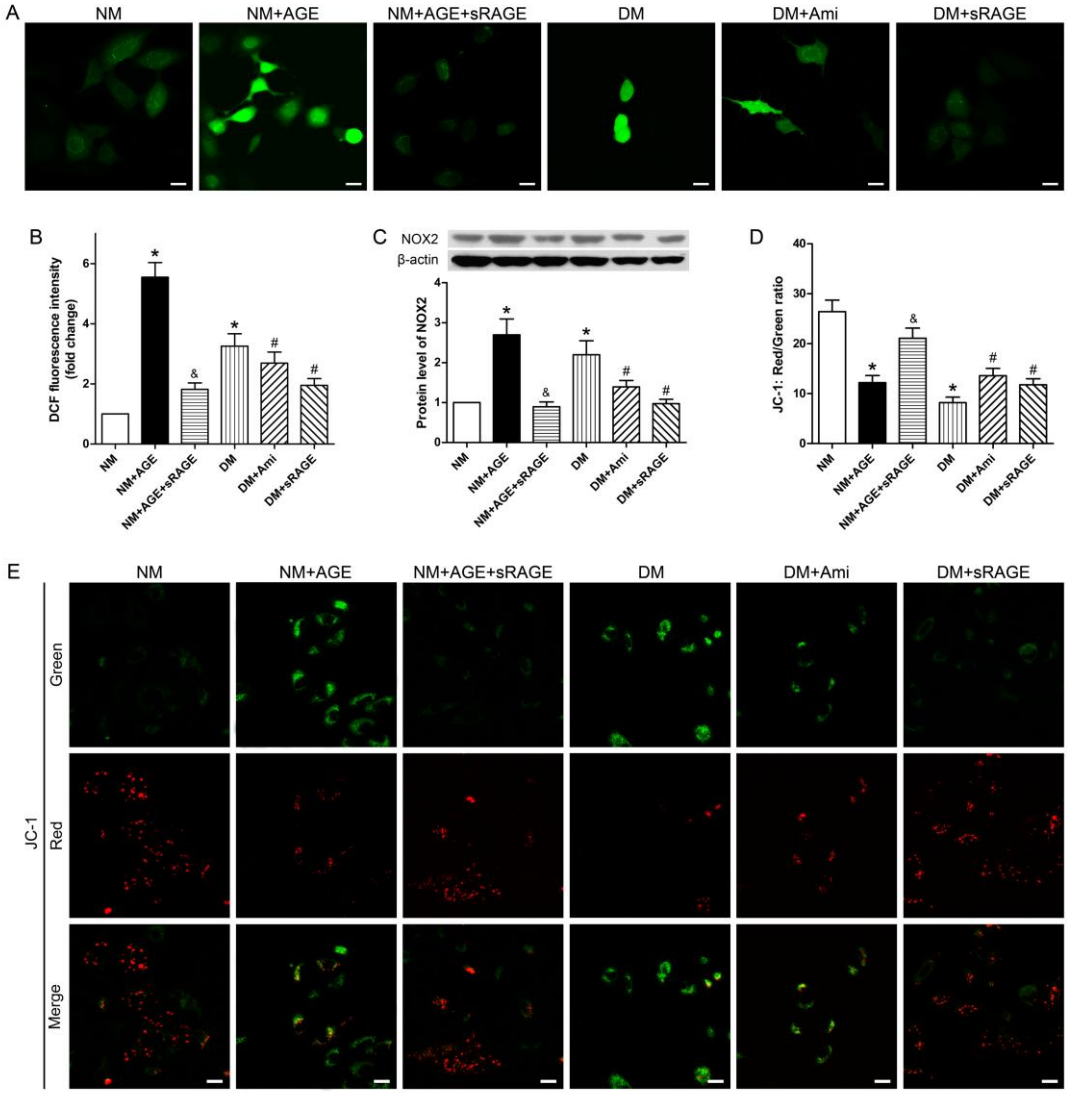

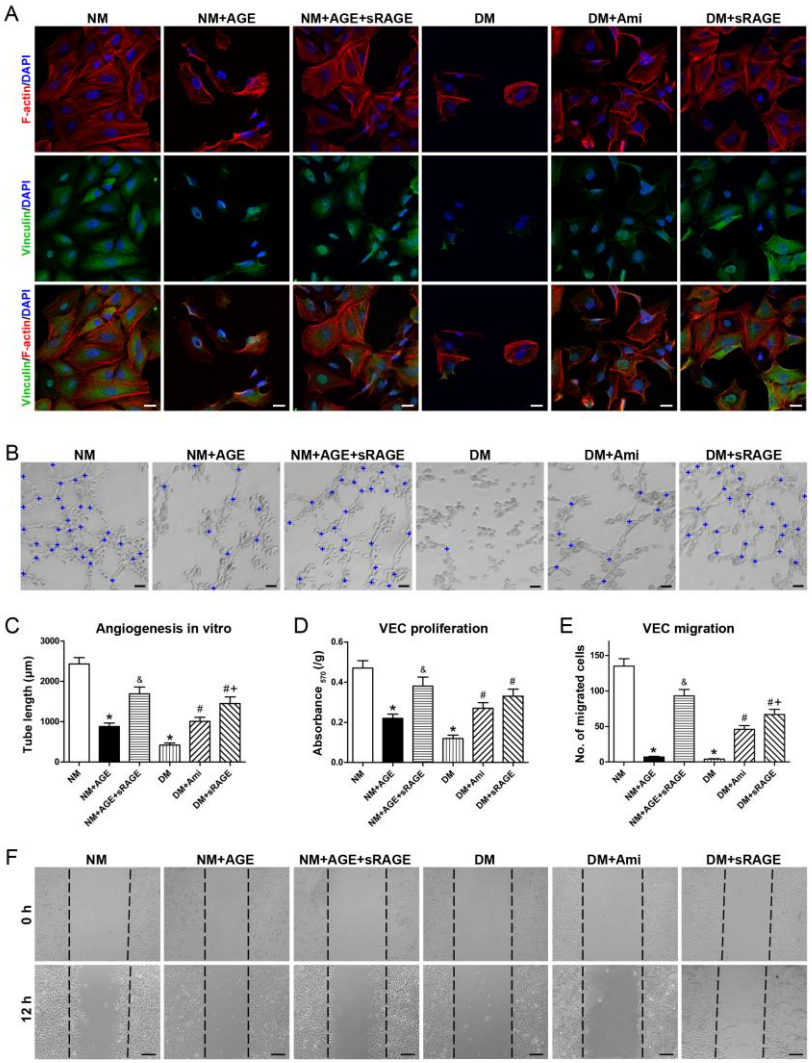

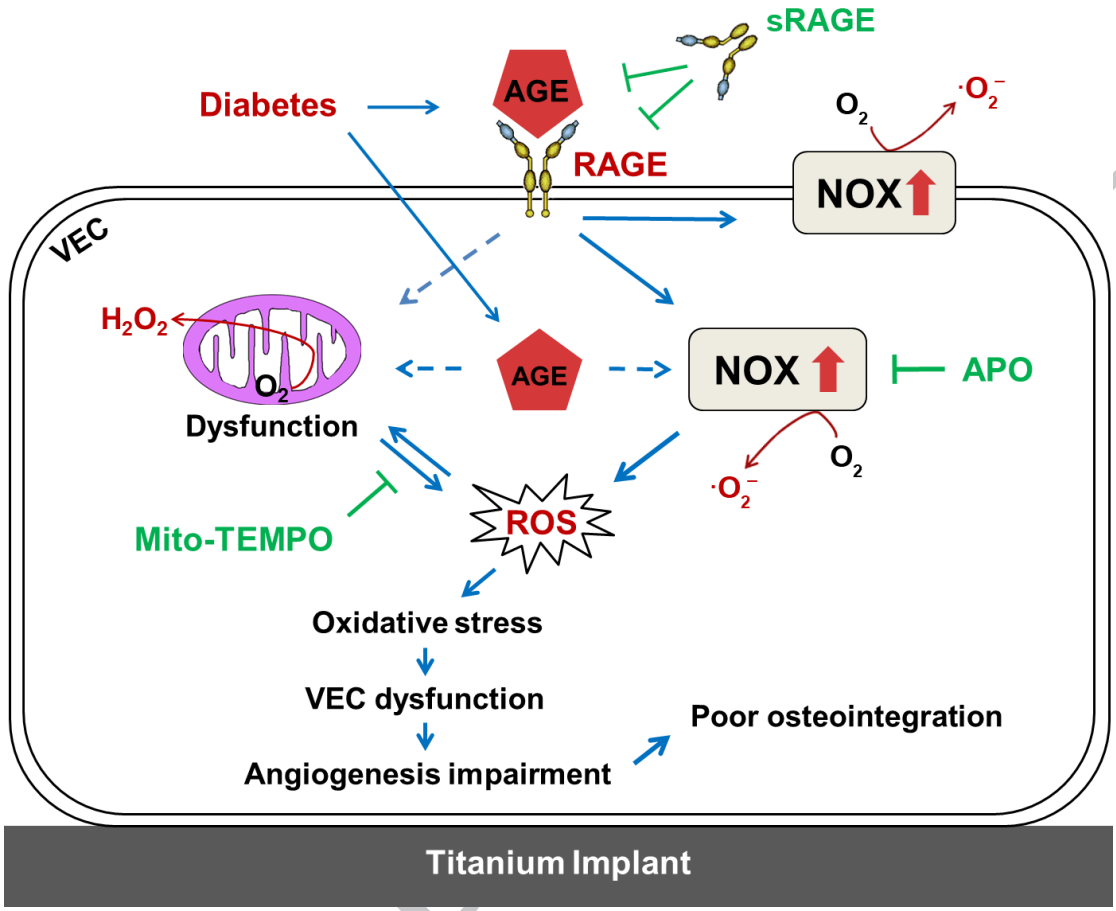
sRAGE
Diabetes
AGE
RAGE
O_2
$\cdot O_2^-$
NOX
VEC
H_2O_2
O_2
Dysfunction
AGE
NOX
APO
O_2
$\cdot O_2^-$
Mito-TEMPO
ROS
Oxidative stress
VEC dysfunction
Angiogenesis impairment
Poor osteointegration
Titanium Implant

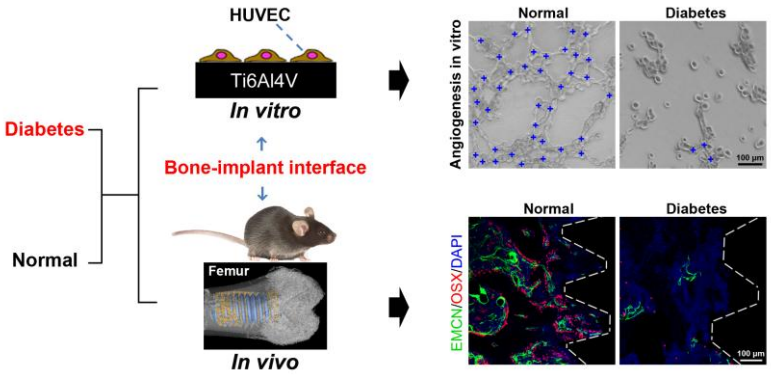

Statement of significance

The high failure rate of bone implants in diabetic patients causes patients terrible pain and limits the clinical application of implant materials. The mechanism underlying this phenomenon needs elucidation so that it would be possible to develop corresponding solutions. Our study demonstrated that the AGEs-related and NOX-triggered oxidative stress of VEC leads to angiogenesis impairment at the bone-implant interface (BII) in diabetes. These are critical mechanisms underlying the compromised implant osteointegration in diabetic hyperglycemia. These provide new insights into the BII in diseased states and also suggest NOX and AGEs as crucial therapeutic targets for developing novel implant materials which could modulate the oxidative stress on BII to get improved osteointegration and reduced implant failure, especially in diabetic patients.

Table 1. Primers used in qPCR.

Gene	Forward primer sequence (5'-3')	Reverse primer sequence (5'-3')
EMCN	AATACCAGGCATCGTGTCAGT	CCACTTCATGTTTTGGTGTTGTC
Vegf-a	GCACATAGAGAGAATGAGCTTCC	CTCCGCTCTGAACAAGGCT
Nog	GCCAGCACTATCTACACATCC	GCGTCTCGTTCAGATCCTTCTC
Bmp-2	GGGACCCGCTGTCTTCTAGT	TCAACTCAAATTCGCTGAGGAC
Runx2	GACTGTGGTTACCGTCATGGC	ACTTGGTTTTTCATAACAGCGGA
Osterix	GGAAAGGAGGCACAAAGAAGC	CCCCTTAGGCACTAGGAGC
β-actin	GTGACGTTGACATCCGTAAAGA	GCCGGACTCATCGTACTCC